

Launching Focused and Spatially Confined Phonon-Polaritons in Hexagonal Boron Nitride

Bogdan Borodin,^{1,2,*} Sergey Lepeshov,^{3,4} Kenji Watanabe,⁵ Takashi Taniguchi,⁶ and Petr Stepanov^{1,2,†}

¹*Department of Physics and Astronomy, University of Notre Dame, Notre Dame, IN 46556, USA*

²*Stavropoulos Center for Complex Quantum Matter, University of Notre Dame, Notre Dame, IN 46556, USA*

³*Department of Electrical and Photonics Engineering, DTU Electro, Technical University of Denmark, Building 343, DK-2800 Kgs. Lyngby, Denmark.*

⁴*NanoPhoton - Center for Nanophotonics, Technical University of Denmark, Ørsted's Plads 345A, DK-2800 Kgs. Lyngby, Denmark.*

⁵*Research Center for Electronic and Optical Materials, National Institute for Materials Science, 1-1 Namiki, Tsukuba 305-0044, Japan*

⁶*Research Center for Materials Nanoarchitectonics, National Institute for Materials Science, 1-1 Namiki, Tsukuba 305-0044, Japan*

Launching and focusing phonon-polaritons present novel opportunities for low-loss guiding of subdiffractively confined light at the nanoscale. Despite significant efforts to improve control in polaritonic media, focused and spatially confined phonon-polariton waves have only been achieved in the in-plane anisotropic crystals (such as MoO₃) and remain elusive in the in-plane isotropic crystals (such as hexagonal boron nitride). In this study, we present a previously unexplored approach to launching phonon-polaritons by employing hBN subwavelength resonators coupled to gold nanoantennas. The integration of gold nanoantennas enables efficient coupling to the far-field component of mid-infrared light, while the geometry of the resonators defines the wavefront curvature, spatial confinement, and focusing of the launched polaritons. Using standard lithographic protocols, we achieve strong field enhancement and resonant mode localization, generating phonon-polaritons with precise spatial definition. Scattering-type scanning near-field optical microscopy reveals the real-space optical contrast of these modes. This innovative and practical approach introduces a new paradigm for fabricating nanoresonators that actively launch and focus phonon-polaritons, opening avenues for advanced nanophotonic devices.

Introduction. Strong light-matter interactions play a crucial role in well-established photonic devices, such as lasers, integrated photonic circuits, sensors, and hold promise for advancing future photonic quantum technologies, entangled spin-photon interfaces, quantum repeaters, and quantum memories¹. In particular, interactions between photons and phonons, which are quantized vibrations of a crystal lattice, result in the formation of propagating and localized phonon-polaritons (PhPs). PhPs have garnered significant attention as they confine light substantially below the diffraction limit²⁻⁴. PhP resonances occur in various crystalline materials within their Reststrahlen band — a region of the spectrum between transverse (TO) and longitudinal (LO) optical phonons, where the materials exhibit properties of a hyperbolic medium⁵. This enables PhP waveguides and cavities with exceptional electromagnetic confinement in the mid-infrared range (mid-IR) and with remarkably low propagation loss compared to plasmon-polaritons⁶. The mid-IR range of the spectrum is highly sought after due to its potential applications in medical diagnostics^{7,8}, bio- and gas sensing⁹⁻¹¹, LiDaRs for spacecraft¹²⁻¹⁴, optomechanics¹⁵, optical trapping¹⁶, and other fields. To achieve micrometer-scale integration of devices in the mid-IR range, the strong confinement provided by hyperbolic materials is likely the only viable solution.

Hexagonal boron nitride (hBN) is one of the most

promising and technologically accessible materials that provides a hyperbolic optical response in the mid-IR region of the spectrum. hBN is a uniaxial hyperbolic material that exhibits two types of hyperbolic optically active transitions — Type I - 760-820 cm⁻¹ ($\epsilon_{xx} = \epsilon_{yy} > 0; \epsilon_{zz} < 0$) and Type II - 1360-1600 cm⁻¹ ($\epsilon_{xx} = \epsilon_{yy} < 0; \epsilon_{zz} > 0$)^{3,17}, where ϵ_{ij} is the permittivity tensor components. Recent studies have reported on the reliable growth of large-scale high-quality crystals with the possibility to control their isotopic purity¹⁸⁻²⁰. Currently, plasmonic nanoantennas are widely used to couple the far-field component of light with polaritonic systems, facilitating the selective launch of phonon-polaritons (PhPs)²¹⁻²⁴. However, this approach suffers from a critical limitation: the lack of control over the wavefront and spatial confinement of the launched PhPs. While hBN nanocavities exhibit remarkable mid-IR light confinement (down to $\lambda/500$, where λ is the incident wavelength), an extraordinary Purcell factor (up to 10^{12}), and a high quality factor ($Q > 400$), the resonant modes in these cavities remain trapped within the resonators²⁵⁻²⁸. Up to our best knowledge, there has been no demonstration of utilizing these localized modes as sources for focused PhPs. This poses a significant promise to the advancement of PhP-based technologies. In particular, effective control over spatially confined propagation and focusing in uniaxial hyperbolic materials ($\epsilon_{xx} = \epsilon_{yy}$), such as hBN, remains elusive. Although spatially confined PhP focusing along the optical axis has been achieved in biaxial hyperbolic materials like MoO₃²⁹, This method is fundamentally constrained by crystallographic directions, making it unsuitable for arbitrary lensing applications.

* bborodin@nd.edu

† pstepano@nd.edu

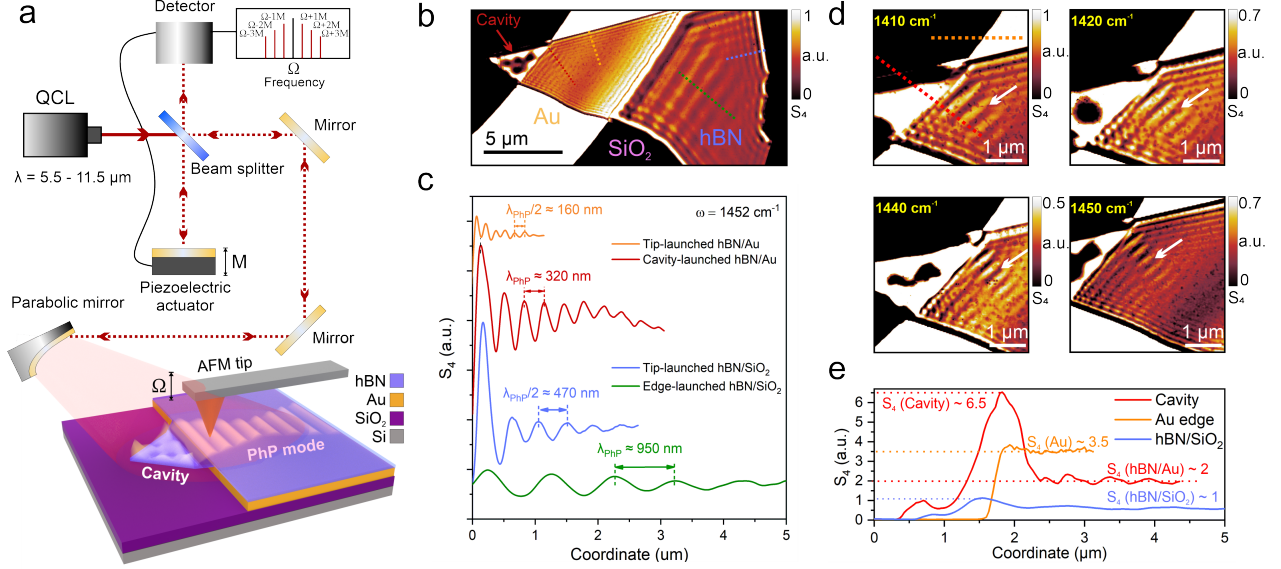


Figure 1. Diversity of PhP waves. **a)** Schematics of the setup for the s-SNOM measurements of PhPs in hBN sub-wavelength resonators. Note that the far-field light covers the majority of the sample's area (spot radius $\geq 10 \mu\text{m}$) **b)** Optical amplitude (S_4) image of the 45-nm-thick hBN flake placed on the pre-patterned Si/SiO₂ substrate with Au stripes. Colored dotted lines indicate line-cuts of various propagating PhP waves. **c)** S_4 profiles taken across corresponding propagating PhP waves. **d)** S-SNOM image of the cavity and propagating PhPs at various excitation wavelengths. **e)** S_4 profiles taken across the Au stripe and the cavity at $\omega = 1410 \text{ cm}^{-1}$.

Here, we demonstrate hBN sub-wavelength resonators coupled to gold nanoantennas, compatible with standard lithographic protocols and capable of launching focused and spatially confined long-lived PhPs. We fabricate sub-wavelength hBN cavities at the edges between Au and Si⁺⁺/SiO₂ (285 nm) substrates. The Au edge serves as a nanoantenna, enabling coupling to the far-field component of light, while the Au/SiO₂ interface acts as a partially transparent wall for PhPs: on the SiO₂ side, it localizes a resonant mode within the cavity, while on the Au side, it promotes the launch of resonantly enhanced PhPs into the hBN bulk. The localized modes exhibit pronounced field enhancement and generate polaritons spatially defined by the cavity dimensions. Using scattering-type scanning near-field optical microscopy (s-SNOM), we visualize the real-space optical contrast and distinguish between cavity-launched (λ_p) and tip-launched ($\lambda_p/2$) modes. The former results from coupling with the far-field component of mid-IR light, which makes a significant contribution to the PhPs launched in this system. The far-field component, resonantly enhanced in the nano-cavities, acquires sufficient momentum to launch polaritons into the bulk of the hBN/Au heterostructures via scattering processes at the SiO₂/Au interface. This approach contrasts with previous demonstrations of focused PhPs, where polaritons in hBN were primarily excited by the s-SNOM tip³⁰. The shapes of our resonators determine the focal points and wavefronts of the PhPs. By fabricating nano-resonators in various shapes, we demonstrate "concave lens"-like and "convex lens"-like focusing. "Concave lens"-like cavities achieve confinement down to $\lambda/55$ at the focal point. Thus, we propose a novel method for launching and focusing spa-

tially confined in-plane PhPs, fully compatible with standard lithographic procedures.

Results. In this work, we study two types of samples: (i) mechanically cleaved hBN crystals (of 30-45 nm thickness) transferred on the pre-patterned Au on Si⁺⁺/SiO₂ (285 nm) substrates as is (see Methods) and (ii) nano-resonators fabricated at the edges between SiO₂ and Au using electron-beam lithography and plasma etching (see the schematics in Fig.1). Fig. 1a shows the measurement scheme for s-SNOM accompanied by the schematics of the fabricated sample. Here, we use a commercially available s-SNOM equipped with PtIr-coated (23 nm thick) AFM tips with the curvature radii less than 25 nm. A tunable ($\lambda = 5.5\text{-}11.5 \mu\text{m}$) mid-infrared quantum cascade laser allows us to cover Type II hyperbolic transition - $1360\text{-}1600 \text{ cm}^{-1}$ ($\epsilon_{xx} = \epsilon_{yy} < 0; \epsilon_{zz} > 0$) (see Methods section for details).

Fig. 1b shows optical amplitude (s_4) versus tip position on a 42-nm-thick hBN flake placed on top of a 50-nm-thick Au stripe at $\omega = 1452 \text{ cm}^{-1}$ (see topography and optical phase data in Extended Data Fig. S1). We focus on three specific regions: i) to the left of the Au stripe, ii) on top of the Au stripe, and iii) to the right of the Au stripe. The first region comprises a triangular hBN piece, where we observe distinct maxima and minima of the optical amplitude (related to the electric field amplitude $(\text{Re } E_z)^2$), characteristic of localized resonant PhP modes²⁸. In the second region, we identify two types of the PhP waves. The first type appears near the edges of the hBN flake (highlighted by the orange dotted line). The second wave emanates from the cavity (red dotted line). In the third region, additional two PhP waves are

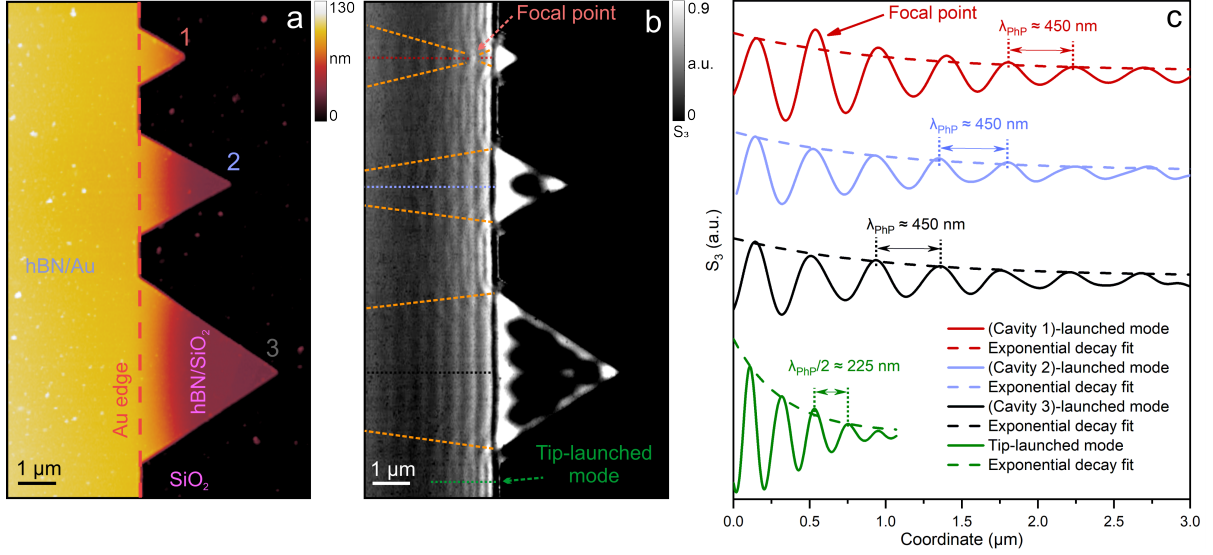


Figure 2. **Focusing of PhPs using patterned nanoresonators.** **a)** AFM topography of the Au edge with the resonators of triangular shapes. The hBN flake thickness is 45 nm. Red dashed line shows the edge between Au and SiO₂. **b)** Experimental s-SNOM amplitude (S_3) map vs. the tip position recorded at $\omega = 1450 \text{ cm}^{-1}$. **c)** s-SNOM amplitude (S_3) profiles taken across cavity-launched waves (red, blue, and black lines) and the hBN flake edge on Au (green line). Dashed lines show exponential decay fit for each curve.

visible. The first wave is positioned near the edges of the hBN flake (blue dotted line). The second wave extends from the edge of the Au stripe to the right across the entire hBN bulk (green dotted line).

The waves, which are localized close to the edge and propagate perpendicularly to it, are the tip-launched PhPs (we do not observe hBN edge-launched fringes in our geometry)³¹. These waves originate from the mid-IR light scattered on the AFM tip. The observed fringes represent only a half-wavelength of the corresponding PhP ($\lambda_{\text{PhP}}/2$) since the detection moves along with the excitation^{32,33}. Based on this, we attribute the orange and the blue PhP waves to the tip-launched modes on Au and SiO₂, respectively.

Fig. 1c shows linecuts taken along the dotted lines in the panel Fig. 1b. As expected, the red and the green curves exhibit doubled wavelengths λ_{PhP} (compared to the tip-launched waves on Au and SiO₂, respectively). Intriguingly, they also demonstrate notably longer propagation lengths. We attribute these PhPs to the nanocavities-launched waves³³. These waves originate from the light scattered at the edge of the Au stripe. In the case of the green curves, the infrared light launches the corresponding PhP in the hBN on SiO₂. For the red curves, we assume that the Au edge launches the PhPs inside the cavity where they localize and enhance, and then it leaks back through the semi-transparent interface into the hBN bulk on Au. We emphasize that the tip-launched PhPs (orange and blue curves) only exist when the AFM tip is present in the measurement setup, while the PhPs, indicated by the red and green lines, couple to the far-field light and exist as long as there is far-field light excitation.

Fig. 1d shows a set of zoomed-in maps of the cavity-

launched wave at various excitation wavelengths. The launched PhP (white arrow) moves and shrinks along with the resonant maximum position inside the cavity (see the detailed investigation of the dispersion in Extended Data Fig. S2). Fig. 1e shows optical amplitude profiles taken along the red and the orange lines in Fig. 1d at $\omega = 1410 \text{ cm}^{-1}$. We find that the electric field is significantly enhanced inside the cavity exhibiting a two-fold larger reflectivity compared to the bare gold signal (and seven-fold larger compared to hBN/SiO₂ signal). This observation establishes our nanocavities as effective PhP resonators.

To investigate PhP waves' dependence on their shapes and sizes, we utilize a standard electron beam lithography and plasma etching (see Methods). We fabricate nanocavities of the desired shapes at the edges of gold patterns. Fig. 2a shows a topography of one of our samples. Attributed to an exceptional alignment (within $\sim 10 \text{ nm}$) between the e-beam lithography steps, we create the matching edges between the patterned hBN and the Au substrates. This allows us to avoid unwanted leakages of the polaritonic modes away from our nanocavities. On the left hand side of the orange dashed line, a 45 nm thick hBN flake covers a 50 nm thick Au stripe. On the right hand side, the patterned hBN triangles hang from the Au edge and lie down on the SiO₂ substrate (note a smooth hBN topography height transition across the Au/SiO₂ edge). Respectively, Fig. 2b shows an experimental s-SNOM amplitude (S_3) taken at $\omega = 1450 \text{ cm}^{-1}$ (see its dispersion and the analogous set of data for a 31 nm thick hBN in Extended Data Fig. S3 and S4, respectively). Inside the cavities, the scattered signal maxima confirm the field localization and enhancement.

Similar to the case in Fig. 1, two different PhP waves

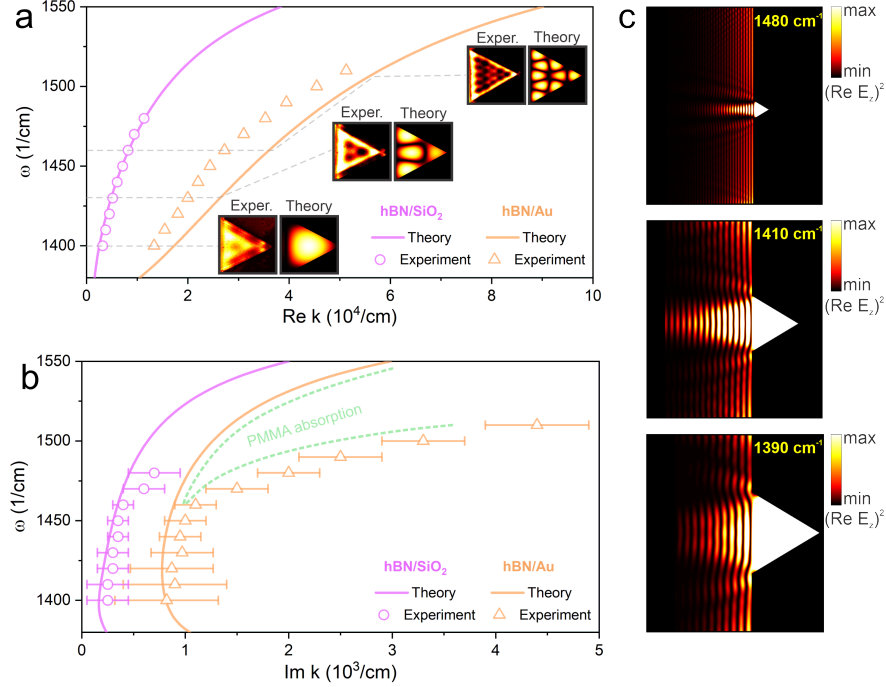


Figure 3. **Numerical simulations of PhPs alongside comparisons to experimental data.** a) Numerically calculated dispersion of propagating PhP modes generated at the hBN/SiO₂ and hBN/Au interfaces (solid lines) compared to the experiment (symbols). Insets show the experimental s-SNOM optical amplitude (S_4) maps and the theoretical spatial distributions of $(\text{Re } E_z)^2$ in triangular cavities, for the wavelength indicated by the grey dashed lines. b) Numerically and experimentally obtained dispersion of the attenuation constant ($\text{Im } k$) for hBN/SiO₂ and hBN/Au interfaces. The error bars indicate the spread of $\text{Im } k$ in the experimental data. c) $(\text{Re } E_z)^2$ in triangular cavities which we experimentally probe in Fig. 2. The distributions are taken at the cavity's resonant frequencies. All calculations are done for hBN thickness of 45 nm.

can be observed. The shorter one is a tip-launched PhP (indicated by a green arrow with the wavelength $\lambda_{\text{PhP}}/2$). This wave results from mid-infrared light scattered by the AFM tip, which excites phonon-polaritons that propagate toward the edge of the sample, reflect back, and interfere with themselves^{32,34–37}. Interestingly, we observe the second PhP wave originating from the cavities themselves. Here, we observe that the peak-to-peak distance corresponds to the whole λ_{PhP} . It is worth noting that $\lambda_{\text{PhP}}/2$ fringes are completely suppressed in front of the cavities, and only λ_{PhP} fringes are observed.

Importantly, we find that the cavity-launched PhPs acquire well-defined focal points. For the top cavity (cavity 1), the PhP shrinks before and expands after the focal point (marked by the red arrow). The lateral size of the focal point corresponds to a confinement of $\lambda/25$. For the bottom two cavities, PhPs shrink with the distance away from the cavities towards their focal points that are located outside of the detectable regions. The orange dashed lines serve as guides to the eye, indicating the boundaries of the cavity-launched phonon-polaritons. At the focal point, we identify a "hot spot" that corresponds to the electric field node. Consequently, the PhP's width and the focal point location can be varied by the size of a cavity.

Fig. 2c shows linecuts taken across the dashed lines in Fig. 2b (solid lines) and their exponential decay fits (dashed lines). Tip-launched PhPs show a strong first

peak of oscillation but a fast decay of the PhP amplitude due to high losses³⁸. On the contrary, cavity-launched PhPs exhibit a stable amplitude of oscillations with the considerably slow decay. As a result, pronounced optical amplitude oscillations of the cavity-launched PhPs are propagating more than three times farther than the tip-launched PhPs.

To characterize the decay rate quantitatively, we fit the amplitude of oscillations using an exponential decay law $A = A_0 e^{-\kappa x} + A_f$, where A_0 and A_f are the fitting parameters related to the initial and the final amplitude values, x is the coordinate of the tip position, and κ is the attenuation constant (equals to $2 \times \text{Im } k$). The larger the value of κ , the faster the damping. For the tip-launched PhPs on Au, we obtain $\text{Im } k \sim 3.1 \times 10^3 \text{ cm}^{-1}$. For the all cavity-launched PhPs, $\text{Im } k$ acquires several times smaller values $\text{Im } k \sim 1.0 \times 10^3 \text{ cm}^{-1}$. Thus, the fitting demonstrates that the cavity-launched PhP quenches considerably slower than the ordinary tip-launched PhP.

Numerical simulations. To shed light on the physics of PhPs in our cavities and to establish an approach for their engineering with the desirable characteristics, we build a theoretical model that predicts optical properties of PhPs and effectively replicates the PhP dynamics in the triangular cavities observed in the experiment. Fig. 3a shows the dispersion of the propagation constant ($\text{Re } k$) of the PhP guided modes at the hBN/SiO₂ and hBN/Au interfaces. The thickness of the hBN flake is

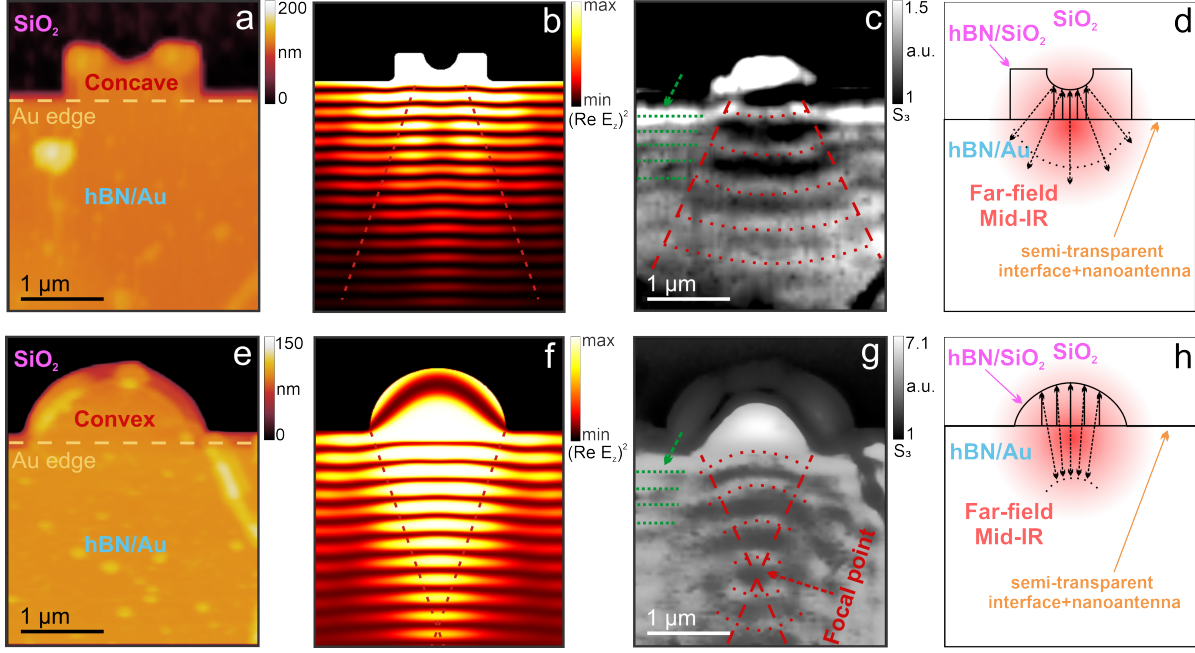


Figure 4. **Concave- and convex-type PhPs focusing.** **a, b, c, d)** AFM topography, numerical modeling, s-SNOM optical amplitude (S_3) maps and the schematics of "concave lens"-like cavity. **e, f, g, h)** Same data for the "convex lens"-like cavity. Light yellow dashed lines show the edge between Au and SiO_2 . Experimental s-SNOM optical amplitude (S_3) maps recorded at $\omega = 1410 \text{ cm}^{-1}$. The thickness of hBN is 55 nm. Red dashed lines are a guide for eyes indicating boundaries of cavity-launched polaritons. Dotted lines highlight maxima of optical amplitude for cavity-launched and tip-launched PhPs. Green lines demonstrate tip-launched PhP waves.

45 nm. The numerically calculated dispersion appears in a good agreement with the data extracted from the experiment albeit the dispersion for the hBN/Au interface appears to be slightly off. We attribute it to the buckling of the hBN flakes on the Au edge and to the surface roughness of Au; both can create gaps between hBN and Au that reduce the effective refractive index at the interface.

Fig. 3b shows the dispersion of attenuation constant $\text{Im } k$ and compares it to the experimental data on the decay rate $\kappa = 2 \times \text{Im } k$. The numerical and experimental attenuation constants well-agree with each other between 1400 cm^{-1} and 1460 cm^{-1} but diverge at the frequencies above 1460 cm^{-1} . We attribute this divergence to the absorption on PMMA (e-beam lithography resist) residues that remain on the sample surface after the fabrication process. In this spectral range, PMMA exhibits stronger absorption with an increase in wavenumber^{39,40}. See more data on the dispersion, refractive index and the attenuation constant for the 31- and 42-nm thick hBN in Extended Data Fig. S5 and S6. We use the complex effective refractive index extracted from the numerical data in Fig. 3a,b to construct a 2D model. This model captures the PhP wave dynamics in the cavities and waveguides formed at the hBN/ SiO_2 and hBN/Au interfaces, correspondingly. As can be seen from the insets in Fig. 3b, the simulated field distributions are in good agreement with the experimental optical amplitude maps. However, in the experiment, the optical amplitude along the gold edge is noticeably higher, which can also be attributed to

the buckling effect that cannot be accounted for in our 2D model. Fig. 3c demonstrates the spatial distributions of the PhPs localized in the triangular hBN/ SiO_2 cavities and propagating in the hBN/Au waveguide. The distributions show that the triangular cavities can support localized PhP modes that "leak" into the hBN/Au environment and that the leaked PhP waves are focused at a distance from the triangle base depending on the triangle size, which is also observed in the experiment (see Fig. 2b). This observation indicates that the optical phenomena in phonon-polaritons excited within a 3D structure can be effectively described by a 2D model.

The schematic analysis of the triangular and rectangular cavities (see Extended Data Fig. S7) shows that the shape of the PhP's wavefront is closely related to the geometry of the cavity. For example, the size of the triangular cavity determines the focal point, while cavity-launched PhPs of rectangular cavities do not shrink and, as a result, do not obtain a focal point. Conclusively, due to a strong confinement, polaritons obey the laws of the wave optics, which brings up an opportunity to realize "concave lens"-like and "convex lens"-like focusing.

PhP lensing. Fig. 4a, 4b, and 4c show the AFM topography, numerically calculated electric field $(\text{Re } E_z)^2$, and the experimental near-field optical amplitude (S_3) of a submicron "concave lens"-like cavity, respectively. This patterned shape exhibits defocusing of the polaritons. We provide an intuitive explanation for this process in Fig. 4d. The PhP waves launched by the Au edge, propagate perpendicular to the Au edge inside the cav-

ity and reflect back from the concave cavity edge. Upon reaching the cavity's edge, they reflect normally to the curvature of the reflecting plane. The negative curvature of the reflecting plane results in the negative curvature of the polariton wavefront and, thus, defocusing.

Figs. 4e-g show a cavity that operates in a "convex lens" regime, focusing polaritons at a point distant from the cavity, similar to the triangular cavities. One can observe a focal point where the curvature of the wavefront changes sign from positive to negative as it passes through the focal point. Fig. 4h illustrates a schematics of the "convex lens"-like focusing. The position of the focal point and the confinement may be adjusted by the size of the cavity. For a $0.6\text{-}\mu\text{m}$ -radius cavity, the confinement reaches $\lambda/55$ (see Extended Data Fig. S8). Furthermore, several cavities launching criss-crossing PhPs can be used for the formation of the interference patterns (see Extended Data Fig. S9) forming a lattice of $(\text{Re } E_z)^2$ minima and maxima with a period equal to the polariton wavelength at the intersection. Thus, using the interference of cavity-launched polaritons with various wavefronts, it is possible to form a variety of polaritonic lattices for structured light-matter interaction and opto-mechanical purposes.

Discussion. To accelerate the technological application of spatially defined PhP modes, it is necessary to find a way to precisely control their spatial distribution and focus them at specific real-space locations. Some substantial progress has been made in tuning and focusing of the PhPs using in-plane anisotropic hyperbolic materials such as MoO_3 ⁴¹⁻⁴³. In the case of the uniaxial hyperbolic hBN crystals, most efforts have involved a use of substrates with an in-plane anisotropy in the relevant spectral ranges⁴⁴⁻⁴⁶. However, the influence of these substrates is generally limited. An elegant solution has been proposed by Chaudhary et. al.³⁰ by using phase-fluid materials ($\text{Ge}_3\text{Sb}_2\text{Te}_6$ on a CaF_2 substrate) that locally change their dielectric constants and thus facilitate polaritonic waveguides and metalenses. However, the focusing effect remained rather hindered and the scalable application is somewhat elusive.

In conclusion, we have developed hBN sub-wavelength resonators that are compatible with standard lithographic techniques, enabling the launch of focused, long-lived PhPs. We fabricate the subwavelength hBN cavities on the interfaces between Au and SiO_2 partially transparent for PhPs. The localized modes showed a significant increase of the electric field and launched polaritons that remain confined in the real-space defined by the shapes and sizes of the cavities. Using s-SNOM, we studied the real-space optical contrast of the cavity-launched PhPs. Based on the PhP's wavelength, we demonstrated coupling to the far-field component of the mid-IR light. The far-field component, which is resonantly enhanced in the cavities, gains enough momentum to launch polaritons into the bulk of the hBN/Au heterostructures through the scattering process at the SiO_2/Au interfaces. The shapes of our resonators determine the focal point location as well as the wavefront shapes. By creating different forms of nano-resonators, we showed a focusing effect sim-

ilar to a "concave lens" and a "convex lens." In particular, the "concave lens"-like cavities enable field confinement down to $\lambda/55$ at the focal points. By this, we realize a novel technique for generating and focusing spatially confined easy-plane PhPs compatible with the standard silicon technology.

METHODS

Device fabrication.

$\text{Si}^{++}/\text{SiO}_2$ substrates were pre-patterned using standard photolithography and metal deposition procedures. For photolithography, SUSS MicroTec MJB4 mask aligner and SPR-700 photoresist were used. After the photoresist development, we deposited metal (Ti/Au, 10/50 nm) using the Oerlikon 450B electron beam vacuum deposition system.

hBN flakes were prepared via mechanical exfoliation using PDMS adhesive tapes and were transferred on Si/SiO_2 substrates for selection. Relying on optical contrast, we selected flakes of suitable thicknesses and transferred them on the pre-patterned $\text{Si}^{++}/\text{SiO}_2$ substrates using the PMDS/PC dry transfer method^{47,48}.

For the cavity fabrication, we used the Raith EBPG5200 electron beam lithographer and PMMA 950 A4 e-beam resist. After the resist development, exposed hBN was etched out using Oxford ICP-RIE plasma etcher with CHF_3 plasma source (40 sscm, 90 mTorr, 60 W).

Near-field optical measurements.

We used a commercially available scattering-type scanning near-field microscope (s-SNOM) developed by Neaspec/Attocube (cryo-neasCOPE) with a pseudo-heterodyne mode to detect a background-free optical response ($\Omega \pm NM$) using the decoupled optical amplitude and phase⁴⁹⁻⁵¹. PtIr-coated AFM tips (Nanoworld, 23 nm coating) with a resonant frequency ≈ 250 kHz were used to obtain the topography and the optical maps. AFM tips were illuminated by a tunable commercially available mid-infrared quantum cascade laser (QCL) using 1-2 mW of power (MIRcat, $\lambda = 5.5\text{-}11.5\text{ }\mu\text{m}$ from the DRS Daylight Solutions Inc.) All optical measurements presented in the manuscript were obtained on the 3rd or the 4th harmonics (i.e., S_3 and S_4 , respectively) to ensure the background-free detection.

Numerical model

To describe the optical phenomena in PhPs at the hBN/ SiO_2 and hBN/Au interfaces, we employ numerical calculations in COMSOL Multiphysics, Wave Optics module. The dispersions of the propagation and attenuation constants of the PhP modes alongside the complex effective refractive indices of these modes are calculated in a 3-layer structure, where the top layer is presented by air, the second layer is presented by hBN which is an anisotropic (along the hard axis) material with permittivity tensor taken from⁵² and optical axis directed perpendicular to the layers, and the third layer is either SiO_2 or Au with refractive indices taken from^{53,54}. The obtained effective refractive indices are used as refractive indices for hBN/ SiO_2 and hBN/Au domains in the 2D model,

and the surrounding space is treated as a dielectric with a refractive index of 1. As a source for the 2D model, we specify the surface current density at the edges of the hBN/SiO₂, hBN/Au domains, and the surrounding space.

REFERENCES

- [1] Rivera, N. & Kaminer, I. Light-matter interactions with photonic quasiparticles. *Nature Reviews Physics* **2**, 538–561 (2020).
- [2] Henry, C. & Hopfield, J. Raman scattering by polaritons. *Physical Review Letters* **15**, 964 (1965).
- [3] Caldwell, J. D. et al. Sub-diffractive volume-confined polaritons in the natural hyperbolic material hexagonal boron nitride. *Nature communications* **5**, 5221 (2014).
- [4] Li, N. et al. Direct observation of highly confined phonon polaritons in suspended monolayer hexagonal boron nitride. *Nature Materials* **20**, 43–48 (2021).
- [5] Poddubny, A., Iorsh, I., Belov, P. & Kivshar, Y. Hyperbolic metamaterials. *Nature photonics* **7**, 948–957 (2013).
- [6] Giles, A. J. et al. Ultralow-loss polaritons in isotopically pure boron nitride. *Nature materials* **17**, 134–139 (2018).
- [7] Waynant, R. W., Ilev, I. K. & Gannot, I. Mid-infrared laser applications in medicine and biology. *Philosophical Transactions of the Royal Society of London. Series A: Mathematical, Physical and Engineering Sciences* **359**, 635–644 (2001).
- [8] Petrich, W. Mid-infrared and raman spectroscopy for medical diagnostics. *Applied Spectroscopy Reviews* **36**, 181–237 (2001).
- [9] De Bruyne, S., Speckaert, M. M. & Delanghe, J. R. Applications of mid-infrared spectroscopy in the clinical laboratory setting. *Critical reviews in clinical laboratory sciences* **55**, 1–20 (2018).
- [10] Popa, D. & Udreă, F. Towards integrated mid-infrared gas sensors. *Sensors* **19**, 2076 (2019).
- [11] Lambert-Girard, S., Allard, M., Piché, M. & Babin, F. Differential optical absorption spectroscopy lidar for mid-infrared gaseous measurements. *Applied Optics* **54**, 1647–1656 (2015).
- [12] Degtiarev, E. A compact frequency agile mid-infrared airborne lidar. *DTIC Document* (2006).
- [13] Groussin, O. et al. Thermap: a mid-infrared spectrometer for space missions to small bodies in the inner solar system. *Experimental Astronomy* **41**, 95–115 (2016).
- [14] Olsen, K. S. et al. First detection of ozone in the mid-infrared at mars: Implications for methane detection. *Astronomy & Astrophysics* **639**, A141 (2020).
- [15] Chen, W. et al. Continuous-wave frequency upconversion with a molecular optomechanical nanocavity. *Science* **374**, 1264–1267 (2021).
- [16] Zhang, J., Liu, W., Zhu, Z., Yuan, X. & Qin, S. Towards nano-optical tweezers with graphene plasmons: Numerical investigation of trapping 10-nm particles with mid-infrared light. *Scientific reports* **6**, 38086 (2016).
- [17] Duan, J. et al. Launching phonon polaritons by natural boron nitride wrinkles with modifiable dispersion by dielectric environments. *Advanced Materials* **29**, 1702494 (2017).
- [18] Wang, L. et al. Epitaxial growth of a 100-square-centimetre single-crystal hexagonal boron nitride monolayer on copper. *Nature* **570**, 91–95 (2019).
- [19] Liu, S. et al. Single crystal growth of millimeter-sized monoisotopic hexagonal boron nitride. *Chemistry of materials* **30**, 6222–6225 (2018).
- [20] Kubota, Y., Watanabe, K., Tsuda, O. & Taniguchi, T. Deep ultraviolet light-emitting hexagonal boron nitride synthesized at atmospheric pressure. *Science* **317**, 932–934 (2007).
- [21] Ni, G. et al. Long-lived phonon polaritons in hyperbolic materials. *Nano letters* **21**, 5767–5773 (2021).
- [22] Pons-Valencia, P. et al. Launching of hyperbolic phonon-polaritons in h-bn slabs by resonant metal plasmonic antennas. *Nature communications* **10**, 3242 (2019).
- [23] Li, P. et al. Hyperbolic phonon-polaritons in boron nitride for near-field optical imaging and focusing. *Nature communications* **6**, 1–9 (2015).
- [24] Dai, S. et al. Subdiffractive focusing and guiding of polaritonic rays in a natural hyperbolic material. *Nature communications* **6**, 6963 (2015).
- [25] Guo, X. et al. Hyperbolic whispering-gallery phonon polaritons in boron nitride nanotubes. *Nature Nanotechnology* **18**, 529–534 (2023).
- [26] Tamagnone, M. et al. Ultra-confined mid-infrared resonant phonon polaritons in van der waals nanostructures. *Science advances* **4**, eaat7189 (2018).
- [27] Alfaro-Mozaz, F. et al. Nanoimaging of resonating hyperbolic polaritons in linear boron nitride antennas. *Nature communications* **8**, 15624 (2017).
- [28] Herzig Sheinfux, H. et al. High-quality nanocavities through multimodal confinement of hyperbolic polaritons in hexagonal boron nitride. *Nature Materials* 1–7 (2024).
- [29] Zheng, Z. et al. Controlling and focusing in-plane hyperbolic phonon polaritons in α -moo3 with a curved plasmonic antenna. *Advanced Materials* **34**, 2104164 (2022).
- [30] Chaudhary, K. et al. Polariton nanophotonics using phase-change materials. *Nature communications* **10**, 4487 (2019).
- [31] Hu, G., Shen, J., Qiu, C.-W., Alù, A. & Dai, S. Phonon polaritons and hyperbolic response in van der waals materials. *Advanced Optical Materials* **8**, 1901393 (2020).
- [32] Dai, S. et al. Efficiency of launching highly confined polaritons by infrared light incident on a hyperbolic material. *Nano letters* **17**, 5285–5290 (2017).
- [33] Menabde, S. G., Heiden, J. T., Cox, J. D., Mortensen, N. A. & Jang, M. S. Image polaritons in van der waals crystals. *Nanophotonics* **11**, 2433–2452 (2022).
- [34] Dai, S. et al. Tunable phonon polaritons in atomically thin van der waals crystals of boron nitride. *Science* **343**, 1125–1129 (2014).
- [35] Basov, D., Fogler, M. & García de Abajo, F. Polaritons in van der waals materials. *Science* **354**, aag1992 (2016).
- [36] Yoxall, E. et al. Direct observation of ultraslow hyperbolic polariton propagation with negative phase velocity. *Nature Photonics* **9**, 674–678 (2015).
- [37] Woo, H. J. et al. Selective mapping of tip-launched near-field scattering of surface plasmon polaritons for retrieving dispersion relation in silver nanoflakes. *ACS Applied Nano Materials* **6**, 2560–2568 (2023).
- [38] Guan, F. et al. Compensating losses in polariton propagation with synthesized complex frequency excitation. *Nature Materials* **23**, 506–511 (2024).
- [39] Blümel, R., Bağcıoğlu, M., Lukacs, R. & Kohler, A. Infrared refractive index dispersion of polymethyl methacrylate spheres from mie ripples in fourier-transform infrared microscopy extinction spectra. *JOSA A* **33**, 1687–1696 (2016).
- [40] Tsuda, S., Yamaguchi, S., Kanamori, Y. & Yugami, H. Spectral and angular shaping of infrared radiation in a polymer resonator with molecular vibrational modes. *Optics Express* **26**, 6899–6915 (2018).

- [41] Ma, W. et al. Ghost hyperbolic surface polaritons in bulk anisotropic crystals. *Nature* **596**, 362–366 (2021).
- [42] Chen, M. et al. Configurable phonon polaritons in twisted α -moo3. *Nature materials* **19**, 1307–1311 (2020).
- [43] Qu, Y. et al. Tunable planar focusing based on hyperbolic phonon polaritons in α -moo3. *Advanced Materials* **34**, 2105590 (2022).
- [44] Chaudhary, K. et al. Engineering phonon polaritons in van der waals heterostructures to enhance in-plane optical anisotropy. *Science Advances* **5**, eaau7171 (2019).
- [45] Gong, Y. et al. Dispersion engineering of in-plane anisotropic phonon polaritons in hbn/te van der waals heterostructures. *Advanced Optical Materials* 2302804 (2024).
- [46] Hajian, H. et al. Tunable plasmon-phonon polaritons in anisotropic 2d materials on hexagonal boron nitride. *Nanophotonics* **9**, 3909–3920 (2020).
- [47] Wang, L. et al. One-dimensional electrical contact to a two-dimensional material. *Science* **342**, 614–617 (2013).
- [48] Purdie, D. G. et al. Cleaning interfaces in layered materials heterostructures. *Nature communications* **9**, 5387 (2018).
- [49] Ocelic, N., Huber, A. & Hillenbrand, R. Pseudo-heterodyne detection for background-free near-field spectroscopy. *Applied Physics Letters* **89** (2006).
- [50] Moreno, C., Alda, J., Kinzel, E. & Boreman, G. Phase imaging and detection in pseudo-heterodyne scattering scanning near-field optical microscopy measurements. *Applied optics* **56**, 1037–1045 (2017).
- [51] Keilmann, F. & Hillenbrand, R. Near-field microscopy by elastic light scattering from a tip. *Philosophical Transactions of the Royal Society of London. Series A: Mathematical, Physical and Engineering Sciences* **362**, 787–805 (2004).
- [52] Kumar, A., Low, T., Fung, K. H., Avouris, P. & Fang, N. X. Tunable light–matter interaction and the role of hyperbolicity in graphene–hbn system. *Nano letters* **15**, 3172–3180 (2015).
- [53] Kischkat, J. et al. Mid-infrared optical properties of thin films of aluminum oxide, titanium dioxide, silicon dioxide, aluminum nitride, and silicon nitride. *Applied optics* **51**, 6789–6798 (2012).
- [54] Babar, S. & Weaver, J. Optical constants of cu, ag, and au revisited. *Applied Optics* **54**, 477–481 (2015).

ACKNOWLEDGEMENTS

We thank Andrey Bogdanov, Lorenzo Orsini, Frank H. L. Koppens and Hanan Herzig Sheinfux for helpful discussions. The authors thank Morten R. Eskildsen for his assistance in setting up the experiment. P.S. acknowledges support from the start-up fund provided by the University of Notre Dame (#373837). K.W. and T.T. acknowledge support from the JSPS KAKENHI (Grant Numbers 21H05233 and 23H02052) and World Premier International Research Center Initiative (WPI), MEXT, Japan.

AUTHOR CONTRIBUTIONS

P.S. and B.B. conceived and designed the experiment. B.B. fabricated samples and performed the measurements. The data were analyzed and interpreted by B.B., S.L. and P.S. The hBN crystals were provided by K.W. and T.T. S.L. performed the numerical calculations. B.B., S.L., and P.S. wrote the manuscript. P.S. supervised the work.

COMPETING FINANCIAL INTERESTS

The authors declare no competing financial interests.

DATA AVAILABILITY STATEMENT

The data that support the findings of this study is available from the corresponding authors upon reasonable request.

Extended Data: Launching Focused Phonon-Polaritons Via Hexagonal Boron Nitride Subwavelength Resonators

Bogdan Borodin,^{1,2,*} Sergey Lepeshov,^{3,4} Kenji Watanabe,⁵ Takashi Taniguchi,⁶ and Petr Stepanov^{1,2,†}

¹Department of Physics and Astronomy, University of Notre Dame, Notre Dame, IN 46556, USA

²Stavropoulos Center for Complex Quantum Matter, University of Notre Dame, Notre Dame, IN 46556, USA

³Department of Electrical and Photonics Engineering, DTU Electro, Technical University of Denmark, Building 343, DK-2800 Kgs. Lyngby, Denmark.

⁴NanoPhoton - Center for Nanophotonics, Technical University of Denmark, Ørstedes Plads 345A, DK-2800 Kgs. Lyngby, Denmark.

⁵Research Center for Functional Materials, National Institute for Materials Science, 1-1 Namiki, Tsukuba 305-0044, Japan

⁶International Center for Materials Nanoarchitectonics, National Institute for Materials Science, 1-1 Namiki, Tsukuba 305-0044, Japan

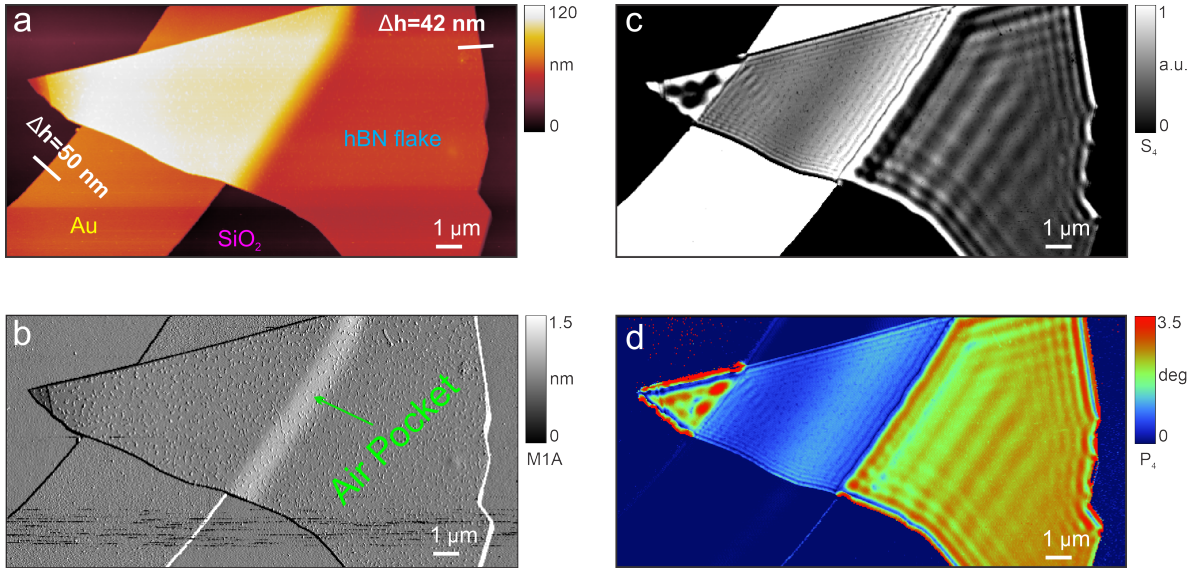


Fig. S1. **Additional data on the as-transferred hBN flake on Au.** **a)** AFM topography map. **b)** Mechanical amplitude map. **c)** Optical amplitude (S_4) map at $\omega = 1450 \text{ cm}^{-1}$. **d)** Optical phase (P_4) map at $\omega = 1450 \text{ cm}^{-1}$.

* bborodin@nd.edu

† pstepano@nd.edu

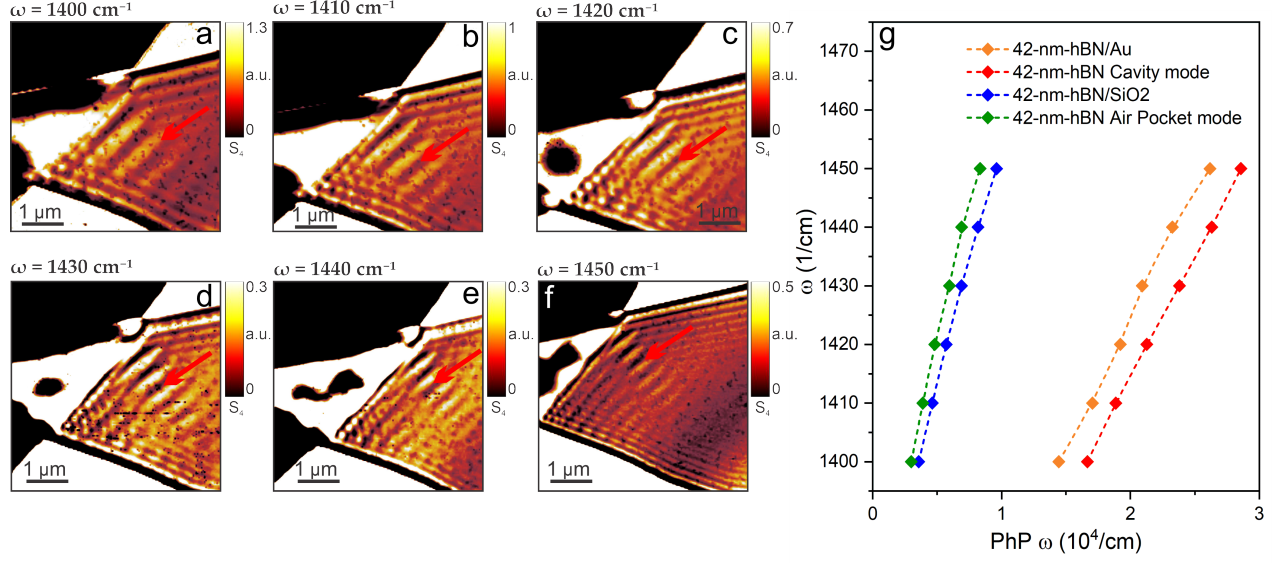


Fig. S2. **PhP dispersion in naturally fabricated hBN cavity.** a-f) Optical amplitude (S_4) maps at various excitation $\omega = 1400\text{-}1450 \text{ cm}^{-1}$. The red arrow shows the cavity-launched mode. g) Dispersion relations of different phonon-polariton modes. The green and blue lines correspond to the modes shown in Fig. 1b of the main text.

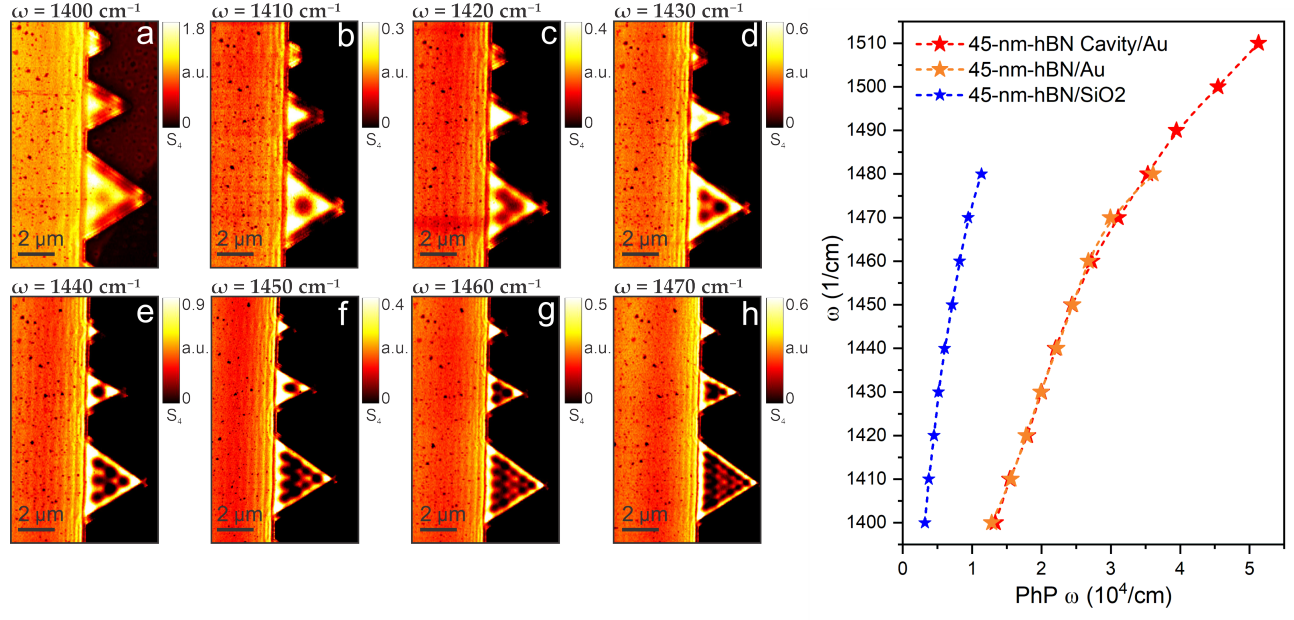


Fig. S3. **PhP dispersion in 45-nm-thick hBN cavities.** a-h) Optical amplitude (S_4) maps at various excitation $\omega = 1400\text{-}1470 \text{ cm}^{-1}$ for 45-nm-thick cavities. i) Dispersion of phonon-polariton modes for the 45-nm-thick flake and cavities.

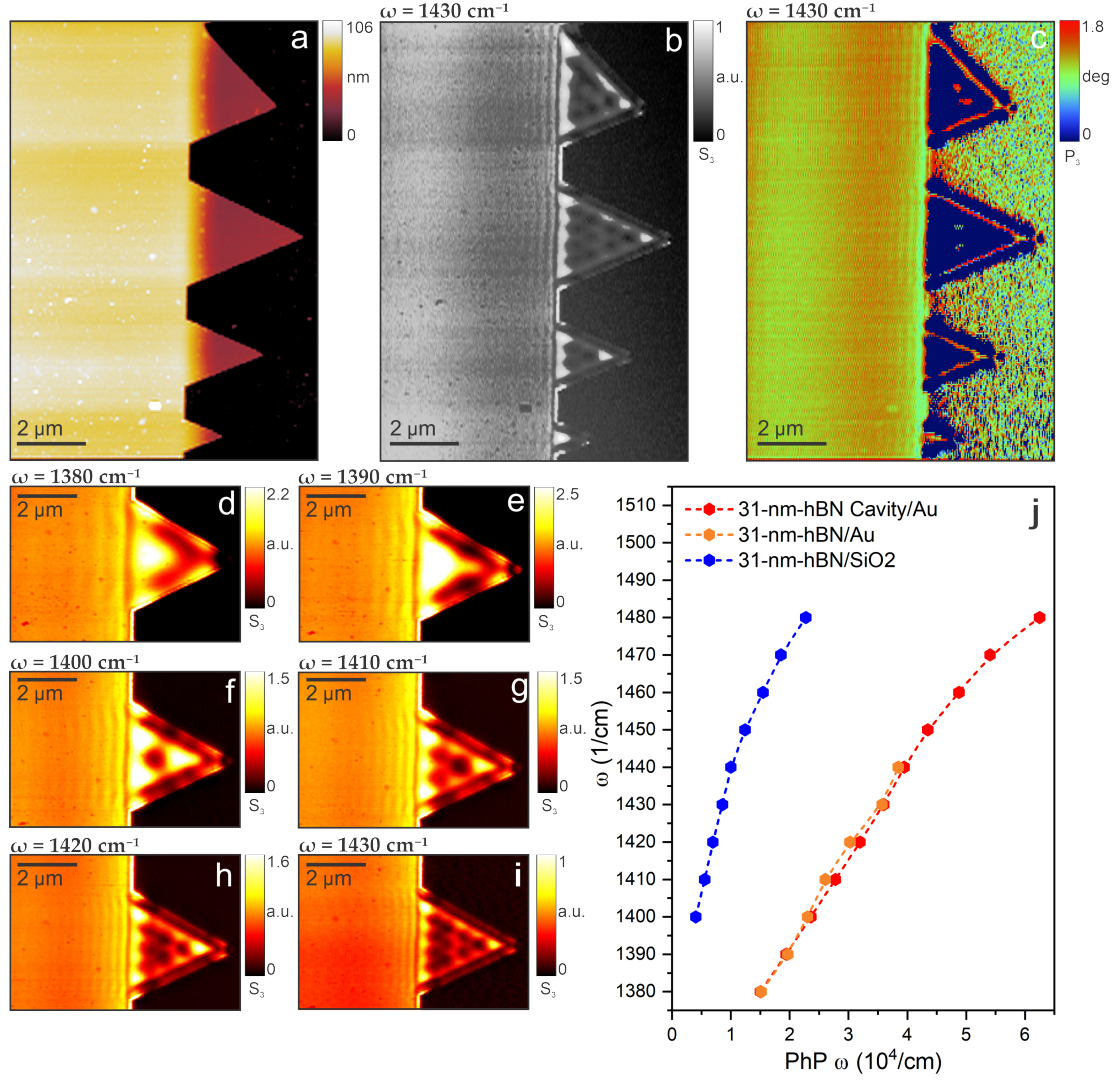


Fig. S4. **31-nm-thick hBN flake and cavities.** a) AFM topography of the cavities. b) Optical amplitude (S_3) map at $\omega = 1430 \text{ cm}^{-1}$. c) Optical phase (P_3) map at $\omega = 1430 \text{ cm}^{-1}$. d-i) Optical amplitude (S_3) maps at various excitation $\omega = 1380\text{-}1430 \text{ cm}^{-1}$ for the second from the top cavity. j) Dispersion of the phonon-polariton modes in the 31-nm-thick flake and cavities.

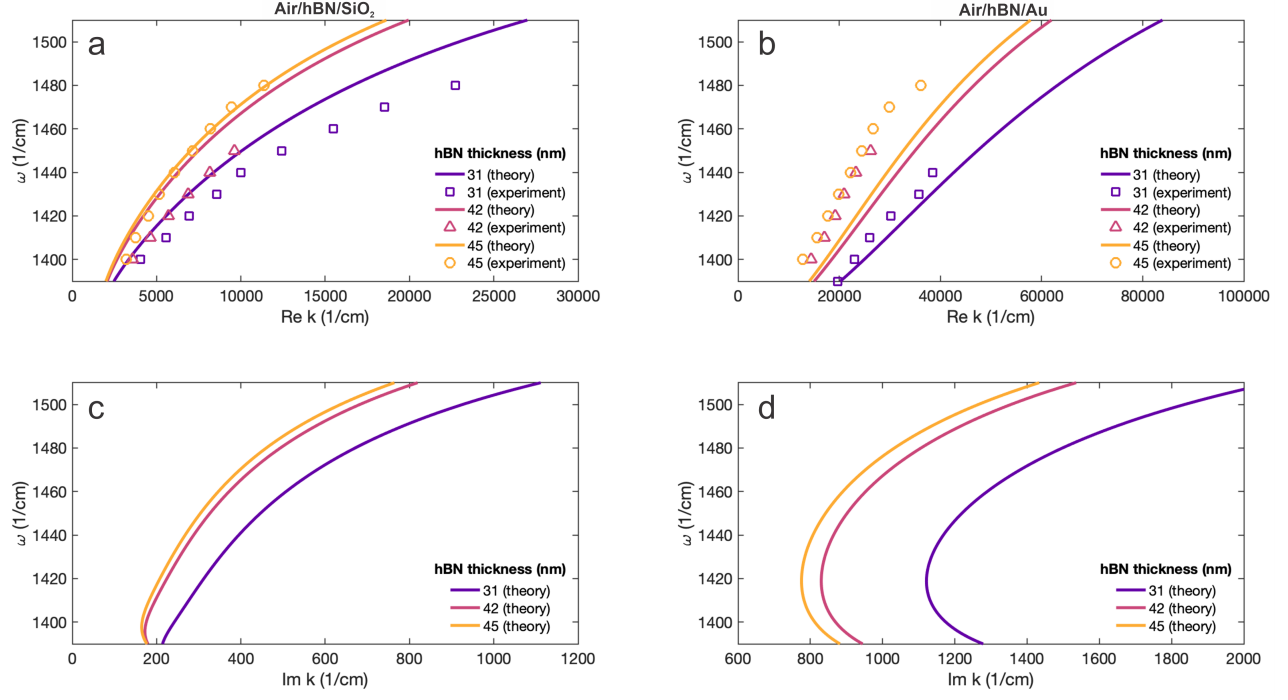


Fig. S5. **Additional data on comparison between the experiment and numerical simulations.** **a, b)** Comparisons between theoretical and experimental dispersions of propagation constants of the PhPs at hBN/SiO₂ and hBN/Au interfaces for the hBN thicknesses of 31, 42, and 45 nm. **c, d)** Dispersions of attenuation constants for the same interfaces.

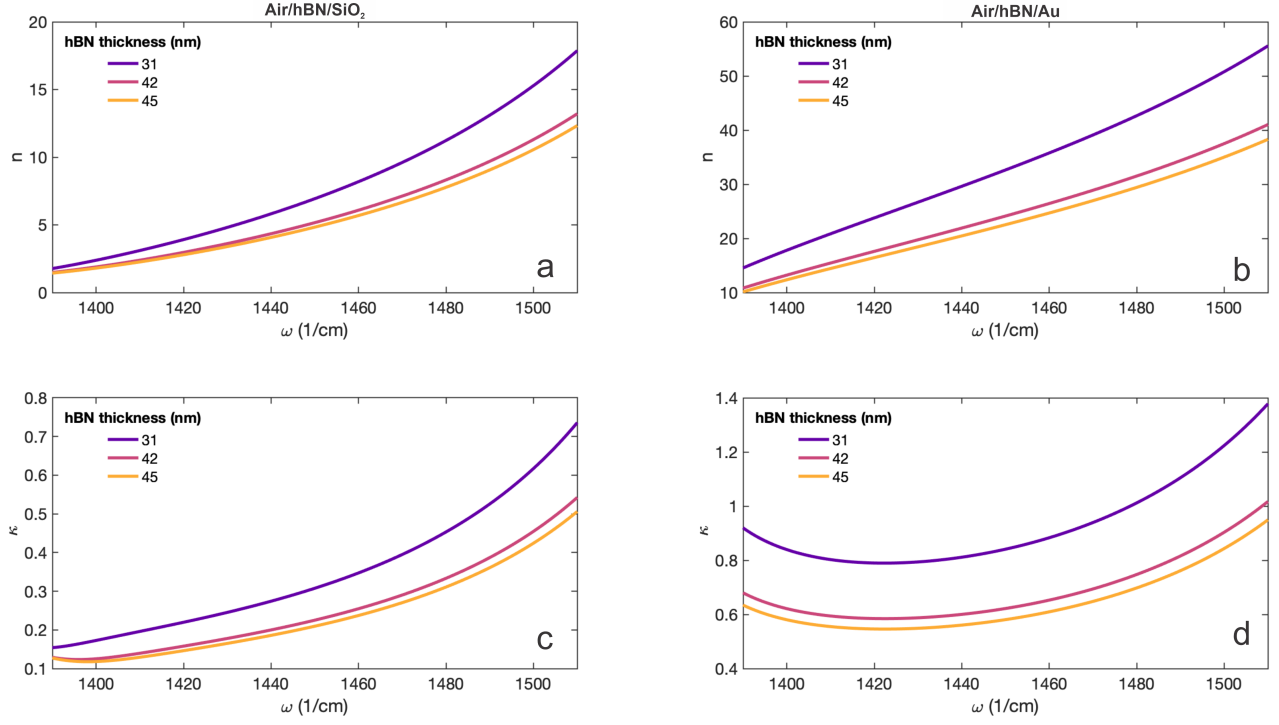


Fig. S6. **Theory.** **a, b)** Refractive indexes (n) of the PhPs at hBN/SiO₂ and hBN/Au interfaces for the hBN thicknesses of 31, 42, and 45 nm. **c, d)** Attenuation constants (κ) for the same interfaces.

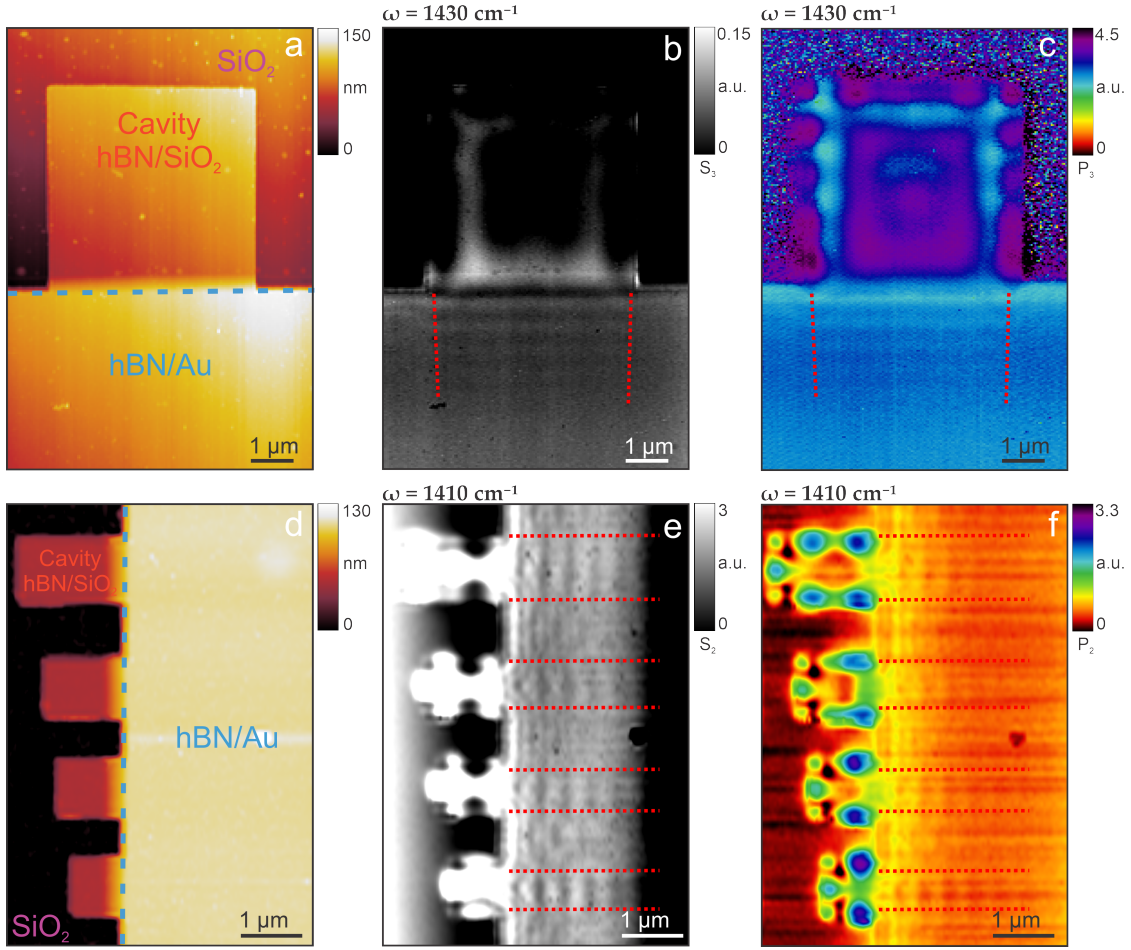


Fig. S7. **Rectangular cavities.** **a)** AFM topography of a large 31-nm-thick cavity. **b)** The corresponding optical amplitude (S_3) map at $\omega = 1430 \text{ cm}^{-1}$. **c)** Optical phase (P_3) map at $\omega = 1430 \text{ cm}^{-1}$. **d)** AFM topography of small 55-nm-thick cavities. **e)** Optical amplitude (S_2) map at $\omega = 1410 \text{ cm}^{-1}$. **f)** Optical phase (P_2) map at $\omega = 1410 \text{ cm}^{-1}$.

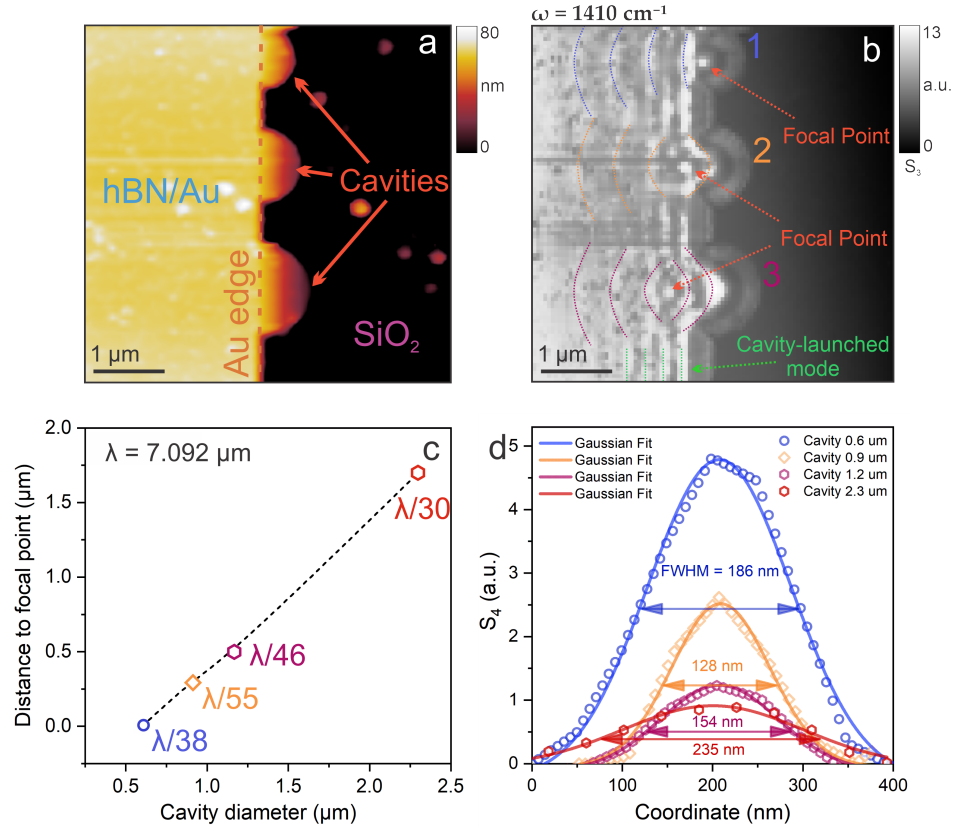


Fig. S8. **55-nm-thick circular cavities.** **a)** AFM topography of the cavities. **b)** Optical amplitude (S_3) map $\omega = 1410 \text{ cm}^{-1}$. **c)** Experimental data on the dependence of the focal distance on the cavity diameter. **d)** Focal point characterization.

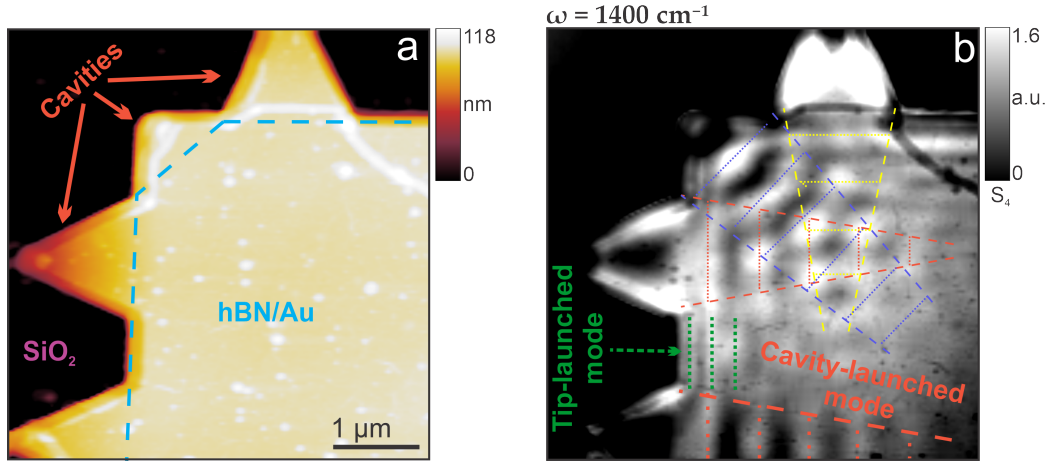


Fig. S9. **55-nm-thick triangular cavities for PhPs interference.** a) AFM topography of the cavities. b) Optical amplitude (S_4) map at $\omega = 1400 \text{ cm}^{-1}$.